LBNL-39031
UC-414

ERNEST ORLANDO LAWRENCE
BERKELEY NATIONAL LABORATORY

Center for Beam Physics Papers

A.M. Sessler, Editor
Accelerator and Fusion Research Division

June 1996
Presented at the
European Particle Accelerator Conference,
Barcelona, Spain,
June 10–14, 1996,
and to be published in
the Proceedings

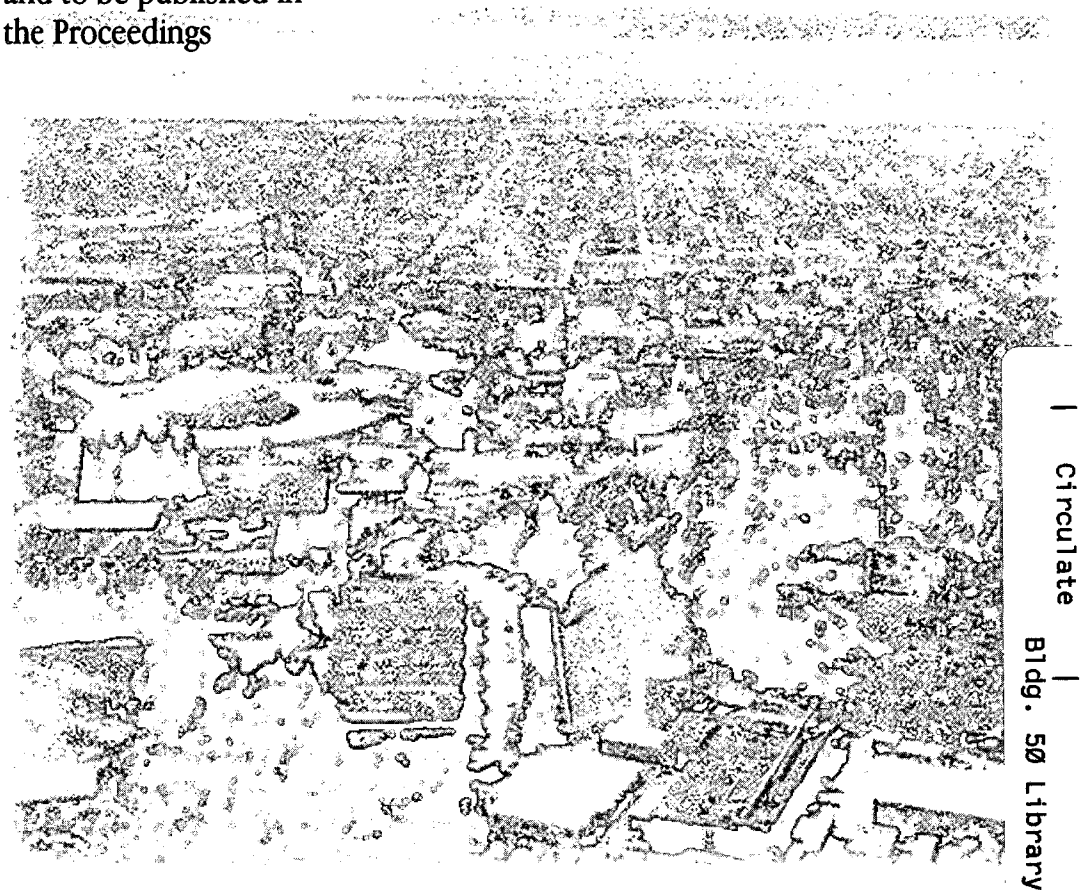

DISCLAIMER

LBL-39031
UC-414

Center for Beam Physics Papers

A.M. Sessler, Editor

Accelerator and Fusion Research Division
Ernest Orlando Lawrence Berkeley National Laboratory
University of California
Berkeley, California 94720

June 1996

This work was supported by the U.S. Department of Energy under Contract No. DE-AC03-76SF00098.

Center for Beam Physics Papers

Contents

LBNL-38935
UC-414

A Second Interaction Region for Gamma-Gamma, Gamma-Electron and Electron-Electron Collision

K.-J. Kim, K. van Bibber, S. Chattopadhyay, W. Fawley,
D. Helm, T. Houck, J. Irwin, D. Klem, D. Meyerhofer,
H. Murayama, M. Perry, M. Ronan, A. Sessler,
T. Takahashi, V. Telnov, A. Weidemann, G. Westenskow,
M. Xie, K. Yokoya, and A. Zholents
Accelerator and Fusion
Research Division

June 1996
Presented at the
European Particle Accelerator Conference,
Barcelona, Spain,
June 10–14, 1996,
and to be published in
the Proceedings

LBNL-38935
UC-414

A Second Interaction Region for Gamma-Gamma, Gamma-Electron and Electron-Electron Collision

K.-J. Kim, K. van Bibber, S. Chattopadhyay, W. Fawley, D. Helm, T. Houck, J. Irwin, D. Klem, D. Meyerhofer, H. Murayama, M. Perry, M. Ronan, A. Sessler, T. Takahashi, V. Telnov, A. Weidemann, G. Westenskow, M. Xie, K. Yokoya, and A. Zholents

(Second Interaction Region Collaboration)

Accelerator and Fusion Research Division
Ernest Orlando Lawrence Berkeley National Laboratory
University of California
Berkeley, California 94720

June 1996

This work was supported by the Director, Office of Energy Research, Office of High Energy and Nuclear Physics, Division of High Energy Physics, of the U.S. Department of Energy under Contract No. DE-AC03-76SF00098.

A SECOND INTERACTION REGION FOR GAMMA-GAMMA, GAMMA-ELECTRON AND ELECTRON-ELECTRON COLLISION†

Kwang-Je Kim
for the Second Interaction Region Collaboration*
Lawrence Berkeley National Laboratory, Berkeley, CA 94720

Abstract

A design of a possible second interaction region (IR2) for $\gamma\gamma$, γe^- and e^-e^- collisions for the next linear collider (NLC) is presented. In the IR2, high energy photon beams are produced via Compton backscattering of focused laser beams by the high energy electron beams and brought into collision with the opposing electron or photon beams. With the goal of obtaining the $\gamma\gamma$ luminosity of about $10^{33}cm^{-2}s^{-1}$ within a 20% bandwidth, we use the electron beams parameters for the NLC e^+e^- design, but modify, the final focus optics. An array of optical mirrors brings the laser beam into a tight focus 5 mm upstream of the interaction point. The laser required must have about a TW of peak power and tens of kW of average power and can be either a solid state laser or a free electron laser.

1 INTRODUCTION

Figure 1 shows the schematic illustration of the IR2. In the following, we describe a summary of a preliminary design of the IR2 for the NLC at 500 GeV energy. A detailed description is given in Appendix B to the Zeroth Order Design Report for the NLC[1]. The major parameters are summarized in Table 1. A review of $\gamma\gamma$ and γe- colliders, machine designs and physics applications, can be found in the proceedings of a workshop at Berkeley[2].

2 THE SCHEME

The laser beam must be chosen to optimize the generation of the γ-rays via Compton scattering at the CP[3]. About n_γ=65% of the high energy electrons are "converted" to γ-photons with the laser parameters in Table 1. The non-linear effects which may spoil the conversion process by shifting the γ-photons to lower energy and producing pairs through non-linear Breit-Wheeler process, etc., are small but not negligible.

The total $\gamma\gamma$ luminosity is approximately given by $n_\gamma^2 \approx 0.4$ times the geometric e^-e^- luminosity. The spectral luminosity depends strongly on the distance b between the CP and the IP; when b=0, it is broadly distributed as a function of the c.m. energy of the two-photon system. As b is increased, the low-energy part of the luminosity spectrum becomes suppressed due to the larger spot size occupied by low-energy photons. For most applications, one would choose $b \approx \gamma\sigma_y^*$, where σ_y^* is the vertical rms spotsize, to obtain a well defined peak of luminosity spectrum at the high-energy end with a bandwidth of about 20% without suffering a large luminosity reduction. In our case, this correspond to b~5mm. The spectral peak at the high-energy end, which is also characterized by a high degree of polarization, acco-

Table 1. Major parameters

Electron beam parameters	
Luminosity goal	~$10^{33}cm^{-2}s^{-1}$ for 20% BW ~5 x $10^{33}cm^{-2}s^{-1}$ for broad band
Beam parameters before FFS	The same as e^+e^- design
Electron energy	250 GeV
Rep. rate	90 bunches separated by 1.4 ns, 180 Hz
Particles per bunch	N_e=0.65 x 10^{10}
Normalized rms emittance	$\gamma\varepsilon_x$= 5 x 10^{-6} mr, $\gamma\varepsilon_y$ = 8 x 10^{-8} mr
Beta function at the IP	$\beta_x^* = \beta_y^* =$ 0.5 mm
Rms spotsize at the IP	$\sigma_x^* = \sigma_y^* =$ 71.5 / 9.04nm
Rms bunch length	σ_z=0.1 mm
Polarization	Fully polarized with helicity switching capability
CP-IP distance	b = 5 mm
Laser parameters	
Wavelength	λ = 1.053 μm
Micropulse energy	A = 1 J
Rms spotsize at waist	$\sigma_{Lx} = \sigma_{Ly}$ = 2.90 μm
Rms angular divergence	$\sigma_{Lx} = \sigma_{Ly}$ = 28.9 mr
Rms micropulse length	σ_{Lz} - 0.23 mm
Peak intensity	≈1 x $10^{18}W/cm^2$
Peak power	0.5 TW
Average power	16.2 kW
Transverse coherence	Near diffraction limited
Polarization	Fully polarized with helicity switching capability

† Work supported by the U.S. Department of Energy under Contract no. DE-AC03-76SF00098.

* K. van Bibber, S. Chattopadhyay, W. Fawley, D. Helm, T. Houck, J. Irwin, K.-J. Kim, D. Klem, D. Meyerhofer, H. Murayama, M. Perry, M. Ronan, A. Sessler, T. Takahashi, V. Telnov, A. Weidemann, G. Westenskow, M. Xie, K. Yokoya, A. Zholents.

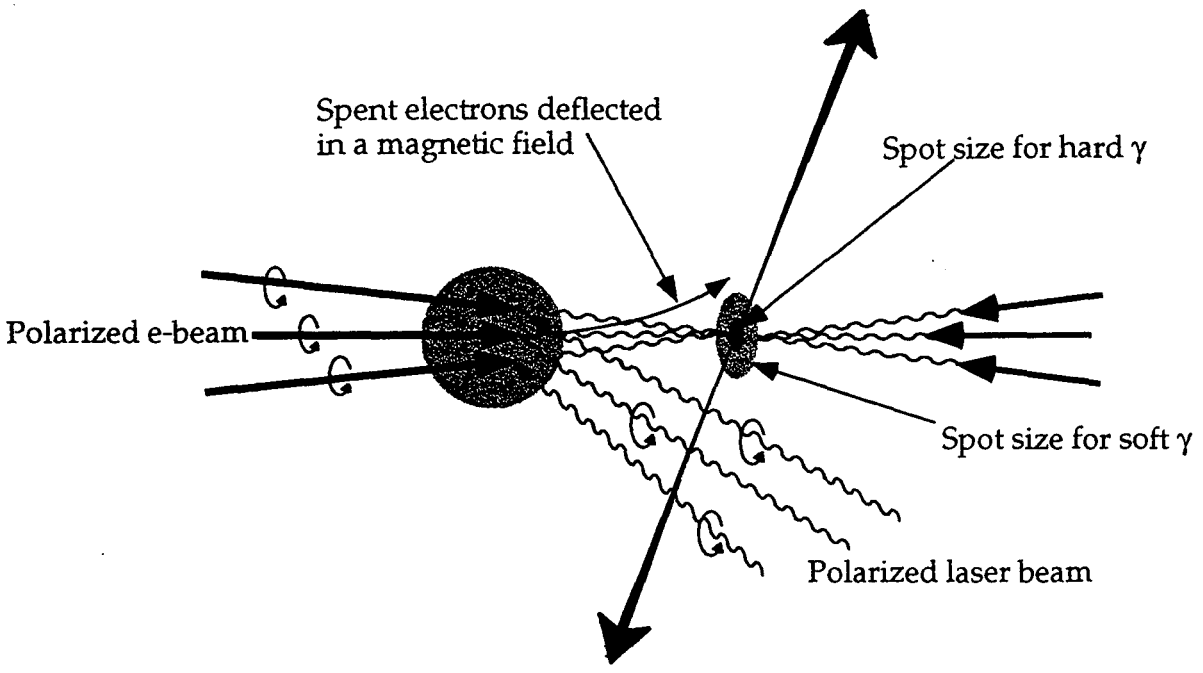

Figure 1: General scheme of gamma-gamma collision.

unts for about 20% of the total $\gamma\gamma$ luminosity, or about 10% of the geometrical e-e- luminosity.

For e^+e^- collisions, the beam spot at the IP is normally designed to be flat to minimize the beamstrahlung effect. In $\gamma\gamma$ collision, the effective vertical beam size is larger than that in the e+e- collisions for a reasonable value of the CP-IP distance b. Thus the FFS for $\gamma\gamma$ collision must provide a value of β_x^* smaller and β_y^* larger than the corresponding values for the e^+e^- design. We aim for $\beta_x^*=\beta_y^*=0.5$mm for the IR2.

The electron beams, if allowed to proceed to the IP, will contribute a large γe background events in $\gamma\gamma$ collisions. A way to avoid the collision of the spent electron beams would be to sweep them away from the IP by an external magnetic field. The magnetic field should extend longitudinally to about 1 cm with a strength of about 1 T. Such a magnet could be designed with a pulsed conductor[4].

3 LUMINOSITY CALCULATIONS

In our preliminary calculation, we have used Telnov's code extensively, which includes the multiple scattering effects in linear approximation and the same-profile approximation for Compton scattering at CP, deflection by external magnetic field and synchrotron radiation in the region between the CP and the IP, the beamstrahlung and the coherent pair production at the IP. A similar code has been assembled by Takahashi[5] based on Ohgaki's Compton conversion package and ABEL[6]. A more refined code incorporating Yokoya's non-linear Compton conversion and the ABEL-MOD[7] is being assembled as a collaborative effect between Hiroshima University, KEK, SLAC and LBNL. This code is referred to as CAIN 1.1. Recently, Yokoya has written a new code, named CAIN 2.0[6].

The results of luminosity calculations can be summarized as follows: We have considered the cases for the collisions at various vertical offset Δy without the sweeping magnet, and the case where there is a 1-T sweeping magnet. The distance between the CP and the IP is taken to be 7.8mm for the latter case. The $\gamma\gamma$ luminosity at high energy end, $z>0.65$, is about 10% of the geometric luminosity. Here z is the invariant mass of the colliding system/energy of the incoming electrons. A significant fraction of the total $\gamma\gamma$ luminosity is therefore in the low-energy region, and arises from the collisions of the beamstrahlung photons generated at the IP by the interaction of the spent electron beams. The luminosity distributions are not a very sensitive function of the offset Δy. The $\gamma\gamma$ luminosity at high energy end ($z>0.65$) is practically constant. Therefore the tolerance on Δy is rather relaxed; Δy up to about $1\sigma_y^*$ does not degrade the collision performance. The background from the low energy $\gamma\gamma$ or γe- luminosities are significantly reduced when the sweeping magnet is employed.

4 LASER OPTICAL PATH

Figure 2 illustrates a possible mirror arrangement for the $\gamma\gamma$ collision region of the NLC. The figure shows the inner radius of the vertex chamber surrounding the IP, the conical mask, the quadrupole holders indicated by two cylinders, the incoming electron beam path indicated by a line nearly parallel to the axis, and the outgoing, disrupted electron beam path indicated by a narrow cone emanating from the IP next to the incoming beam path. The small elliptical objects are the mirrors. One of the laser beams

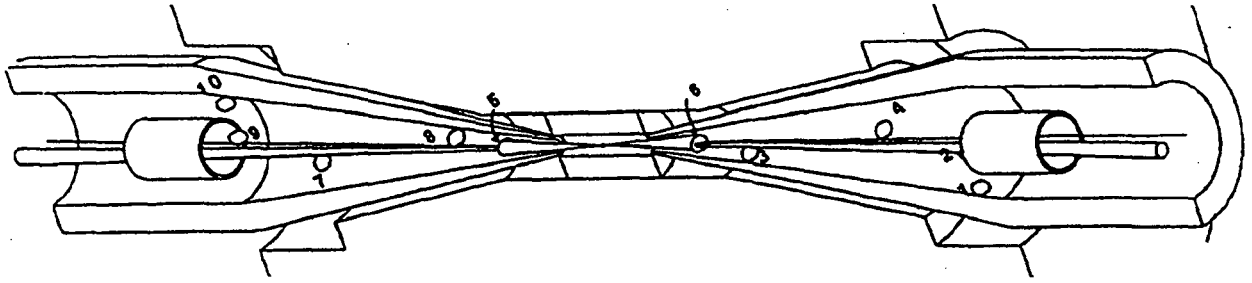

Figure 2: A possible mirror arrangement for the gamma-gamma collision.

enters from the right, and reflected by mirrors in sequence indicated by the numbers. The laser beam avoids the mirror 6 standing between the mirrors 4 and 5 by forming a focus a small distance away from the edge of mirror 6. The beam fills mirror 5 with a near uniform intensity profile, and focus on the CP with a f/7 optics facing the incoming electron beam from the right. Mirror 5 has two holes, a small one for the incoming electron beam and a larger one to accommodate the 10 mr angular cone of the outgoing disrupted electron beam. The laser beam further propagates and fills mirror 6, reflected and focused now to a spot a small distance away from the bottom edge of mirror 5 propagates further to mirrors 7, 8, 9, and 10, and exits to the left. Another laser beam enters from the left following a path symmetric to the beam coming from the right, nearly overlapping the exiting beam.

The mirrors will be of dielectric material with suitable multilayer coatings developed for high power laser systems. A laser path arrangement in which a laser pulse is reused several times will greatly reduce the optical power requirement. Practical implementation of these ideas need to be worked out.

5 ELECTRON FINAL FOCUS SYSTEM

The goal of the FFS for the IR2 is to produce $\beta_x^*=\beta_y^*=0.5$mm, as explained in Section 2. As a first attempt to design the final focus system for $\gamma\gamma$ collisions, kept chromaticity of the final focus doublet close to the chromaticity of the e^+e^- final focus. Thus, with $L^*=2$m, the minimum beam-stay-clear requirement of $10\sigma_{x,y}$, and the maximum pole-tip field in the permanent magnet quadrupoles of 1.35 T, we arrived at reasonable doublet parameters, the quadrupole nearest to the IP being of the F-type. However, the current version of the $\gamma\gamma$ final focus system has $\beta_x^*=0.9$mm and $\beta_y^*=0.7$mm. The increase of the beam spot size at the IP due to the Oide effect is negligible. Following a standard approach to the chromaticity compensation the length FFS is 1600m. Efforts to find smaller b* values resulted in higher x and y chromaticities, implying a greater sensitivity to the quadrupole placement tolerance and also a greater complexity and length of the FFS. By increasing the overall length of the Final Focus section to 1750m, we found a solution giving $\beta_x^*=\beta_y^*=0.5$mm with the energy bandwidth about $\pm 0.5\%$.

6 LASER TECHNOLOGY

While the energy, pulse duration, and focusing can be met with currently operating lasers, based on the chirped pulse amplification technique[9,10], these lasers have not yet met the average power requirements. The average power of high peak power systems has, however, been increasing rapidly recently, driven by activities such as the Isotope Separation program at LLNL and facilitated by the development of high power laser diode pump sources. It is expected that the system requirements will be met with a series of 1-kW, diode-pumped, solid-state, chirped pulse amplification laser systems. These unit cells will be fed by a single, phase-locked oscillator to insure timing stability.

There are several options for the 1 kW unit cell: 1) direct, diode-pumped Nd:Glass based lasers incorporating advanced athermal glass, 2) direct, diode-pumped, broad-bandwidth crystals specially engineered for high average power applications (e.g., Yb:S-FAP or others) and, 3) two-stage laser-pumped lasers such as a long pulse ($\approx$10 ns) neodymium based laser pumping a short-pulse Ti:Sapphire laser.

Free-electron lasers (FEL) are another option for photon colliders, and they are especially interesting for higher energy colliders, where the required wavelength of the laser is longer than ~1 μm, for which solid-state lasers do not presently exist. A scheme based on the chirped pulse amplification in a high-gain FEL driven by an induction linac appears promising[11].

REFERENCES

[1] ZDR Report for NLC, SLAC, May 1996.
[2] Nucl. Instr. Meth. A 355, 1-194 (1995).
[3] V. Telnov, Nucl. Instr. Meth. A 355, 3 (1995)
[4] G. Silvestrov and V. Telnov, unpublished.
[5] T. Takahashi, in preparation.
[6] K. Yokoya, KEK-Report 85-9, October 1985.
[7] T.Tauchi, K.Yokoya, P.Chen, Par. Acc.41,29(1993).
[8] User's Manual of CAIN 2.0 (KEK pub. 4/96).
[9] D.Strickland, G.Mourou, Opt. Com.56, 219(1985).
[10] M. Perry and G. Mourou, Science 264, 917 (1994).
[11] K.-J. Kim, M. Xie and A. Sessler, LBL-37094.

LBNL-38955
UC-414

Constraints on Laser-Driven Accelerators for a High-Energy Linear Collider

J.S. Wurtele and A.M. Sessler
Accelerator and Fusion Research Division

June 1996
Presented at the
European Particle Accelerator Conference,
Barcelona, Spain,
June 10–14, 1996,
and to be published in
the Proceedings

CONSTRAINTS ON LASER-DRIVEN ACCELERATORS FOR A HIGH-ENERGY LINEAR COLLIDER*

J.S. Wurtele and A.M. Sessler
Center for Beam Physics
Lawrence Berkeley National Laboratory
Berkeley, CA 94720

Abstract

General considerations of the requirements for a high energy linear collider (here, to be specific, taken to be 1 TeV on 1 TeV) are applied to free-space laser and laser/plasma accelerators. It is shown that the requirements impose very severe constraints upon the new accelerators--so severe, that it seems unlikely that these necessary criteria can be met in the foreseeable future.

1 INTRODUCTION

Over the last two decades much work has been done -- both theoretically and experimentally -- on the acceleration of particles by means of lasers. Considerable progress has been made in the theoretical understanding of the complicated phenomena associated with the interaction of lasers and plasmas, in numerical modeling of such phenomena, in experimental studies, and in the development of lasers. It is correct to characterize the field as having advanced very significantly during the last decades.

Part of the motivation for the study of laser acceleration has been the application of this method to high energy linear colliders. There are, of course, other applications, but the possible use of these new techniques in high energy physics remains a major interest, and motivating force, for the effort. It is this application that we want to examine in the present report.

We consider, to be specific, a 1 TeV x 1 TeV linear collider. Actually, such a device can, most likely, be achieved with "conventional technology", or with only slightly non-conventional technology such as that in the two-beam accelerator, but higher energy is even more daunting.

In this Report we delineate, in Section II, general considerations having to do with luminosity, beamstrahlung, and wall-plug power. This allows us to derive diverse parameters of the accelerated beam. In Section III we consider acceleration in a vacuum. In Section IV we consider plasma accelerators which consist either of acceleration in a uniform plasma or acceleration in a plasma channel. Finally, in Section V we present a discussion.

*Work supported by the Director, Office of Energy Research, Office of High Energy and Nuclear Physics, High Energy Division, of the U.S. Department of Energy under Contract no. DE-AC03-76SF00098.

2 COLLIDER REQUIREMENTS

The requirements of high energy physics are, for our purposes, simply summarized by the luminosity and the beamstrahlung energy spread of the device. Expressions for these quantities are well-known [1] and are:

$$L = \frac{f N^2}{4\pi \sigma_y^{*2} R} \tag{1}$$

$$\delta = \frac{0.88 r_e^3 N^2 \gamma}{R^2 \sigma_y^{*2} \sigma_z} \tag{2}$$

where f is the effective frequency of the collider (rep. rate x bunch number), N is the number of particles in a bunch, σ_y^* is the rms transverse dimension at the interaction point, R is the ratio of horizontal to vertical size of the beam, r_e is the classical particle radius, σ_z is the longitudinal rms dimension of the bunch, and the beam energy is characterized by γ. The collider requires an operating power which is simply:

$$P_b = 2\gamma mc^2 N f = \eta P_w \tag{3}$$

where the efficiency η is defined in terms of the wall-plug power, P_w.

Since γ, L, and δ are given by the high energy physics requirements and Pw is given by economic considerations, it is convenient to express the unknown quantities, N, σ_y^*, σ_z, R, and f, in terms of the independent quantities. We find, having put in convenient units:

$$\frac{N}{\sigma_z}\left[\mathrm{cm}^{-1}\right] = \left(6.4 \times 10^{10}\right)\left(\frac{\delta \eta P_w(\mathrm{GW}) R}{L\left[10^{35}\right] E^2(\mathrm{TeV})}\right) \tag{4}$$

$$f[\mathrm{MHz}] = .05 \frac{L\left[10^{35}\right] E(\mathrm{TeV})}{\delta \sigma_z[\mathrm{cm}] R} \tag{5}$$

$$\sigma_y^*\,[\mathrm{nm}] \approx 126\sqrt{\delta\sigma_z\,(\mathrm{cm})}\;\frac{\eta P_w\,(\mathrm{GW})}{L\left[10^{35}\right]E^{3/2}\,[\mathrm{TeV}]} \qquad (6)$$

In these expressions σ_z must scale roughly with the acceleration wavelength λ_{acc} (either the laser wavelength in a vacuum acceleration or the plasma wavelength in a plasma accelerator).

Table 1
Two parameter sets both of which achieve the HEP requirements and one that does not (for δ)

		Laser Plasma	Vacuum Laser	Vacuum Laser
Assume	E (TeV)	1	1	1
	L (cm^{-2}-s^{-1})	10^{35}	10^{35}	10^{35}
	δ	0.1	0.1	10.0
	ηP_w (GW)	0.02	0.02	0.02
	σ_z (μm)	10	0.1	0.1
	R	100	100	100
Then	N/σ_z (cm^{-1})	1.3×10^{10}	1.3×10^{10}	1.3×10^{12}
	N	1.3×10^{7}	1.3×10^{5}	1.3×10^{7}
	σ_y^* (cm)	2.5×10^{-9}	2.5×10^{-10}	2.5×10^{-9}
	f (Mhz)	4.9	490	4.9
Assume	$\lambda_{acc}=10\sigma_z$ (μm)	100	1	1
	E_z (GeV/m)	10	1	1
	$\beta^*=\sigma_z$ (μm)	10	0.1	0.1
	ℓ/a	—	10	10
Then	n_p (cm^{-3})	1.1×10^{17}	—	—
	$\frac{\delta n_p}{n_p}$	0.1	—	—
	r_b (μm)	2.3×10^{-3}	—	—
	$\frac{r_b\omega_p}{c}$	10^{-4}	—	—
	$e_N=\gamma\varepsilon=\gamma\sigma_y^{*2}/\beta^*$ (m)	1.3×10^{-10}	1.3×10^{-10}	1.3×10^{-8}
	ΔE (MeV)	—	4.8×10^{-3}	0.48

3 VACUUM ACCELERATORS

There are two general types of vacuum accelerators. The first uses external magnetic fields, or pulses of laser power, to provide transverse bending of particles and, therefore, provides continuous acceleration by the laser as in an Inverse Free-Electron Laser.[2] Inevitably, because of the particles bending, they will radiate and they radiate more and more as their energy is increased. Hence there will be some upper limit on energy at which the synchrotron radiation just compensates the laser acceleration. Typically that energy is below 1 TeV and, therefore, this class of accelerators is not of interest for high energy physics.

Acceleration in a vacuum is greatly restricted by the Lawson-Woodward theorem. [3]That theorem states that there is no net energy gain by a particle provided:

1. The region of interaction extends over all space,
2. The laser fields are vacuum fields; i.e., there are no nearby walls,
3. The particle is highly relativistic; i.e., its velocity is essentially unchanged (and c),
4. No static fields are present (so motion is in a straight line)
5. Nonlinear effects are negligible.

Thus vacuum acceleration (for highly relativistic particles) inevitably involves structures (diaphragms) to deflect the laser light and these structures are subject to material damage.[4] In addition, at high beam intensities there are significant wake field effects due to these diaphragms. The wakes are both longitudinal (limiting the acceleration gradient) and transverse (limiting the bunch transverse size).

A representation of one section of a conceptual vacuum accelerator is shown in Fig 1. The sections are necessary so as to have continuous acceleration; that is, to deflect the laser beam, or introduce a new beam with proper phase, when the particle and the light are no longer in accelerating phase. The diaphragm produces a longitudinal wake which means:

$$\Delta E \approx \frac{2Nre}{\sqrt{\pi\sigma_z}}\log\left(\frac{a}{\sigma_y}\right)mc^2 \qquad (7)$$

where ΔE is the energy loss from one diaphragm, a is the radius of the hole in the diaphragm, l is the length of a section, and σ_y is the transverse rms of the electron beam at the diaphragm. The quantity σ_y scales with the laser wavelength, the quantity a is related to the length of a section l, σ_z scales with the laser wavelength and N/σ_z is fixed by collider considerations. In addition, the diaphragm produces a transverse wake and material damage of the diaphragm restricts the power of the laser.

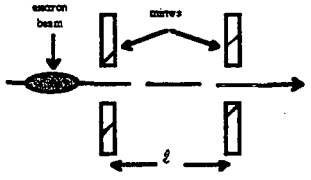

Figure 1. Conceptual picture of one period of a vacuum laser accelerator.

4 PLASMA ACCELERATORS

Plasma accelerators reach high gradients by employing a drive laser pulse or pulses to create a large amplitude plasma wave. Laser-plasma interactions limit the transverse size of the drive laser pulse to be of order the c/ω_p. In this circumstance the accelerating field created in a homogeneous plasma will typically have transverse gradients of order $(\omega_p/c)E_z$, and a transverse component of order $(r\omega_p/c)E_z$, where E_z is the accelerating field. For high gradients, the plasma focusing will dominate any external focusing. Thus the accelerating structure, i.e., the plasma, controls both transverse and longitudinal motion of the accelerated bunch. Alternatively, plasma waves can be driven by a particle bunch, which approach has problems of its own that are not addressed here.

The transverse gradients of the accelerating field, and the strength of the focusing, can be reduced by accelerating in a plasma channel.[5] The channel also acts as an optical fiber, guiding the laser light and allowing for acceleration lengths much greater than a diffraction length. In the hollow plasma channel, the transverse focusing force is reduced by a factor of order γ_g^{-2}, where γ_g is the group velocity of the laser in the plasma channel. The beam radius then increases as $\gamma_g^{1/2}$.

The misalignment of a quadrupole in a conventional linac corresponds to, in a plasma accelerator, a stray electric field in the plasma. The strength of the accelerating field will determine the tranverse focusing strength and thereby the level to which stray fields need to be controlled. These undesirable fields can orginate from laser-plasma instabilities, density inhomogenities, etc. An estimate of the focusing strength in the plasma gives an equilibrium radius in the plasma of $r_b=(\varepsilon\beta_p)^{1/2}$.

The electron beam in the plasma will generate wakes. The higher order mode losses and transverse BBU for the accelerated bunch in the plasma will set constraints on the accelerated current. These effects should be less pronounced in a plasma than in vacuum laser accelerators since the plasma acceleraor has a longer wavelength (and hence wider transverse dimensions) and the plasma is, ideally, homogeneous in the longitudinal direction.

5 DISCUSSION

We now examine the results of collider designs based on the above constraints, as seen in Table 1. We have, arbitrarily, taken the beam power to be 20 MW so that the wall plug power, P_W, depending on the efficiency of the laser-to-particle system, is in the range of hundreds of megawatts which would seem to be about all one could afford. The interesting range of accelerating wavelength can be covered with only two cases, the first--with λ_{acc} = 100 μm--corresponds to a plasma accelerator and the second--with λ_{acc} = 1μm--corresponds to a vacuum accelerator. There really is very little freedom in these choices; they correspond to reasonable plasma densities and reasonable wavelengths for powerful lasers. The choice of accelerating wavelength sets the scale for σ_z; we have choosen it to be 1/10 of of the wavelength.

Column 1 of the Table gives parameters for a plasma accelerator and column 2 gives parameters for vacuum accelerators. As can be seen from the first two columns of the Table, obtaining the desired high energy physics puts very severe requirements on the laser-driven accelerators. Firstly, the repetition rate must be very high and, secondly, the emittance (and consequently the beam size) must be very small. The emittance is two orders of magnitude smaller and the assumed β^* values are one or three orders of magnitude smaller, than are planned for future linear colliders. The first is a technological problem (but not a trivial problem) and the second puts very tight requirements upon component tolerance and component location. Our calculation has been classical, but at the very small σ_y we are considering QED corrections are important even at 1 TeV. Quantum corrections change δ in column 1 of the Table to .02, and δ in column 2 from 0.1 to 0.003. Operation with large quantum effects brings in other complications. Changing parameters so that quantum effects are small furthermore forces one into a regime where wake fields become inportant.

Perhaps one can argue that beamstrahlung is not really a constraint. After all, the concept of plasma compensation [6] has been put forward (but never experimentally established). In order to study that case we present, in column three of Table 1, a situation with vacuum acceleration but beamstrahlung a factor of 100 greater than in the first two columns. The laser accelerator is now less difficult than before (the emittance and associated tolerances are now achievable), but still very difficult to achieve.[7] We are now in a regime where longitudinal wakes are important---with a staging length l=500μm the decelerating gradient is 1GV/m.

We have presented an overall review of the requirements that high energy colliders put upon any laser-driven accelerator. We find that the 1 TeV application is daunting enough, and the application to still higher energy is even more difficult.

Perhaps, it can be argued, imposing collider requirements upon laser accelerators, at a time when the accelerators are still in their infancy, is unfair. On the other hand, serious work on laser accelerators has been in progress for 15 years and, furthermore, often claims are made that seem to ignore--rather than consider and address--the elementary constraints discussed in this paper. We believe that it is important that advocates of laser-driven accelerators, for collider applications, face up to the limits discussed in this paper.

Of course there are other applications of laser-driven accelerators--and many of these are "easier" to achieve that are colliders. These, alone, justify, in our opinion, further work on the subject.

We wish to thank Glen Westenskow for his valuable discussions.

6 REFERENCES

1. R. B. Palmer, Annu. Rev. Nucl. Part. Sci., **40**, 529 (1990).
2. E.D. Courant,C. Pellegrini, and W. Zakowicz,,Phys. Rev. A **32**, 2813 (1985).
3. J.D. Lawson, IEEE Trans. Nucl. Sci. **NS-26**, 4217 (1979); P.M. Woodward, J. IEEE **93**, 1554 (1947).
4. P. Sprangle, E. Esarey, and J. Krall, "Laser Driven Electron Accelerators in Vacuum, Gases and Plasmas", Physics of Plasmas (to be published).
5. G. Shvets, et.al., to appear in IEEE J. Plasma Science, 1996.
6. D.H. Whittum et al, Part. Accel. **34**, 89 (1990).
7. D. Zheng and R. Byer, "Proposed Waveguide Structure for Laser Driven Electron Acceleration", Advanced Accelerator Concepts, AIP Conf. Proc. **335**,156 (1995).

LBNL-38934
UC-414

Progress on the Design of a High Luminosity $\mu^+\mu^-$ Collider

R. Palmer, A. Tollestrup and A. Sessler
Accelerator and Fusion Research Division

June 1996
Presented at the
European Particle Accelerator Conference,
Barcelona, Spain,
June 10–14, 1996,
and to be published in
the Proceedings

Progress on the Design of a High Luminosity $\mu^+\mu^-$ Collider

R. B. Palmer, A. Sessler, and A. Tollestrup
for the Muon Collider Collaboration

Abstract

Parameters are presented for a 2 + 2 TeV muon collider with a luminosity of $\mathcal{L} = 10^{35}\text{cm}^{-2}\text{s}^{-1}$. The design is not optimize for performance, neither for cost; however, it does suffice to allow us to make a credible case that a muon collider is a serious possibility for particle physics, that could open up the realm of physics above the 1 TeV scale, allowing, for example, copious production of supersymmetric particles or a detailed study of the strongly-interacting scenario of electroweak symmetry breaking.

1 INTRODUCTION

This article is a brief summary distilled from the report, Muon-Muon Collider: A Feasibility Study [1] to be presented at the 96 Snowmass Workshop, which contains the collaborative effort of scientists from Brookhaven National Laboratory (BNL), Fermi National Laboratory (Fermilab), Lawrence Berkeley National Laboratory (LBNL), and significant contributions from individual researchers from U.S. universities, SLAC, and KEK.[2]

The muon collider complex consists of components (see Fig. 1) which first produce copious pions, then capture the pions and the resulting muons from their decay; this is followed by an ionization cooling channel to reduce the longitudinal and transverse emittance of the muon beam. The next stage is to accelerate the muons and, finally, inject them into a collider ring wich has a small beta function at the colliding point. This is the first attempt at a point design and it will require further study and individual optimization of components and overall optimization. Tb. 1 shows the main parameters of the muon collider complex. Experimental work will be needed to verify the validity of diverse crucial elements in the design which can be enumerated as:

- ionization cooling channel
- superconducting and/or fast pulsed magnets for the accelerator
- study and modeling of magnets for the collider ring.

Muons because of their large mass compared to an electron, do not produce significant synchrotron radiation. As a result, there is negligible beamstrahlung and high energy collisions are not limited by this phenomena. In addition, muons can be accelerated in circular devices which will be considerably smaller than two full-energy linacs as required in an $e^+ - e^-$ collider. A hadron collider would require a CM energy 5 to 10 times higher than 4 TeV to have an equivalent energy reach. Since the accelerator size is limited by the strength of bending magnets, the hadron collider for the same physics reach would have to be much larger than the muon collider. In addition, muon collisions should be cleaner than hadron collisions.

There are many detailed particle reactions which are open to a muon collider. Most of the physics accesible to an $e^+ - e^-$ collider could be studied in a muon collider. In addition the production of Higgs bosons in the s-channel will allow the measurement of Higgs masses and total widths to high precision; likewise, $t\bar{t}$ and W^+W^- threshold studies would yield m_t and m_W to great accuracy. These reactions are at low center of mass energy (if the MSSM is correct) and the luminosity and $\Delta p/p$ of the beams required for these measurements is detailed in [1]. On the other hand, at 2 + 2 TeV, a luminosity of $\mathcal{L} \approx 10^{35}\,\text{cm}^{-2}\,\text{s}^{-1}$ is desirable for studies such as, the scattering of longitudinal W bosons or the production of heavy scalar particles.[3] Not explored in this work, but worth noting, are the opportunities for muon-proton and muon-heavy ion collisions as well as the enormous richness of such a facility for fixed target physics provided by the intense beams of neutrinos, muons, pions, kaons, antiprotons and spallation neutrons.

To see all the interesting physics described herein requires a careful study of the operation of a detector in the very large background. Three sources of background have been identified:

- The first is from any halo accompanying the muon beams in the collider ring. Very carefully prepared beams will have to be injected and maintained.
- The second is due to the fact that on average 35 % of the muon energy appears in its decay electron. The energy of the electron subsequently is converted into EM showers either from the synchrotron radiation they emit in the collider magnetic field or from direct collision with the sur-

rounding material. The decays that occur as the beams traverse the low beta insert are of particular concern for detector backgrounds.

- A third source of background is $e^+ - e^-$ pair creation from $\mu^+ - \mu^-$ interaction. Studies of how to shield the detector and reduce the background are addressed in the Detector Chapter.[1]

Polarization of the muons allows many very interesting measurements which are discussed in the Physics Chapter.[1] Unlike the electron collider in which the electron beam is highly polarized and the positron beam unpolarized, both muon beams may be partially polarized. It is necessary to select forward moving muons from the pion's decay and thus reduce the available number of muons and hence the luminosity. The necessary machine technology needed to achieve such a collider is discussed in the Option Chapter;[1] at the moment it is not part of our point design, although such capability would almost certainly be incorporated into an actual device.

2 DESCRIPTION OF THE MACHINE

The driver of a muon collider is a 30 GeV proton synchrotron capable of providing 2.5×10^{13} protons per bunch with four bunches per pulse and 15 Hz pulse rate. The repetition rate, but not the number of protons, is beyond that of any existing machine, but not so far beyond as to seem unrealistic. In fact, the criteria are almost met by the design of KAON.[4] The protons are driven into a target, most likely a liquid target, where copious pions are produced (about one pion per proton). Questions of target survivability are discussed in the Target Chapter.[1] The target is surrounded by a 20 T solenoidal field, which is adiabatically matched to a 5 T solenoid in the decay channel. The captured pions have a wide range of energy, with a useful range from 100 MeV up to 1 GeV. A strong phase-rotating rf field is used to reduce this energy spread as well as the longitudinal extent of the beam. This results in approximately, 0.3 muons per proton with mean energy of 150 MeV and a $\pm 20\,\%$ rms energy spread. The muons (about 8×10^{12}) are subsequently cooled by means of ionization cooling (Fig. 2 shows, schematically, emittance reduction due to ionization cooling) which is achieved in a periodic channel consisting of focusing elements, solenoids and/or lithium lenses and absorber at places of small beam size (but corresponding large transverse beam angles) and rf cavities to make up for the energy loss. In some locations along the channel, dispersion is introduced and wedge shaped absorbers are used to produce longitudinal cooling. This is described in the Cooling Chapter.[1] We allow for further loss, beyond natural decay, between the number of captured muons and the final number of muons, coming out of the cooling section is 3×10^{12} per bunch.

After cooling, the muons are accelerated in a cascaded series of recirculating linear accelerators, as described in the Acceleration Systems Chapter.[1] A conventional synchrotron cannot be used as the acceleration is too slow and the muons will decay before reaching the design energy. On the other hand, it is possible to consider synchrotron-like pulsed magnets in the arcs of a recirculator. It should be noted that the primary cost of a muon collider complex is in the acceleration, so care and attention must be devoted to this matter. However, the process is reasonably straight-forward.

The collider ring is injected with two bunches of each sign of 2×10^{12} high energy muons. Approximately 1000 turns occur within a luminosity lifetime, thus making a ring (in contrast with a single collision) advantageous. In order to reach the desired high luminosity, it is necessary to have a very low β^*, of the order of 3 mm, (and associated very large betas in the focusing quadrupoles) at the insertion point.[5] Since the muons only live about 1000 turns, numerical simulations can easily provide us with quantitatively correct information. It is necessary to run the ring nearly isochronously so as to prevent bunch spreading and yet keep the rf impedance low enough as to avoid collective instabilities. Space charge effects, and beam-beam effects, in the collider ring are being studied and some conclusions are presented in the Collider Ring Chapter.[1] Such a ring has never been built, but should be possible to construct and operate.

The muon complex requires numerous superconducting magnets. These are needed in the capture section, in the decay channel, in the arcs of the recirculating accelerators, and in the collider ring. Attention has been given to these magnets, as well as to the very special magnets required for the interaction region, and these various considerations may be found in the appropriate chapters of reference[1].

A study of the scaling laws governing muon colliders is presented in the Options Chapter.[1] Naturally, one would, if the concept is shown to be of interest, initially construct a lower energy machine (perhaps in the hundreds of GeV region) and thus the scaling laws are of special interest. In particular, a lower energy demonstration machine of $\mathcal{L} = 10^{33} cm^{-2} s^{-1}$ at 500 GeV CM energy could serve as a breadboard for exploring the properties and technologies needed for this class of colliders, while providing useful physics.

3 CONCLUSIONS

We suggest that to make sensible decisions about the future, the potential of a muon collider must be explored as rapidly and aggressively as possible. The document[1] of which this paper is a brief summary furnishes a solid base for identifying areas where more

study and/or innovations are needed. In particular, R&D needs to be done related to the muon cooling channel, recirculating superconducting magnets or pulsed magnets for the accelerator in order to arrive at a design that minimizes cost. The magnets for the collider ring have a high heat load from muon decay electrons.

A sustained, extensive and integrated program of component development and optimization will have to be carried out in order to be assured that the design parameters can be attained and the cost minimized. The technology for the most part already exists within the High Energy Physics community and the work should involve the US, Europe, Russia, Japan and the international HEP community as a whole.

4 REFERENCES

[1] "Muon Muon Collider: Feasibility Study", BNL, FNAL, and LBNL Report.

[2] Scientists and institution participants in the collaboration are listed in [1].

[3] V. Barger, New Physics Potential of Muon-Muon Colliders Beam Dynamics and Technology Issues for $\mu^+\mu^-$ Colliders: 9th Advanced ICFA Beam Dynamics Workshop, Montauk, NY, October 15-20, 1995.

[4] Kaon Factory Study, Accelerator Design Report, TRIUMF, Vancouver, B.C., Canada.

[5] A. Garren, et al., Design of the Muon Collider Lattice: Present Status to appear in Proceedings of the Symposium on Physics Potential and Development of $\mu^+\mu^-$ Colliders, San Francisco, CA (1995); Supplement to Nuclear Physics B, to be published.

Table 1: Parameters of Collider Rings

	4 TeV
Beam energy (TeV)	2
Beam γ	19,000
Repetition rate (Hz)	15
Muons per bunch (10^{12})	2
Bunches of each sign	2
rms Norm. emittance ϵ^N ($10^{-6}\pi$ m $-$ rad)	50
Bending Field (T)	9
Circumference (km)	7
Average ring mag. field B (T)	6
Effective turns before decay	900
β^* at intersection (mm)	3
rms beam size at I.P. (μm)	2.8
Luminosity ($cm^{-2}s^{-1}$)	10^{35}

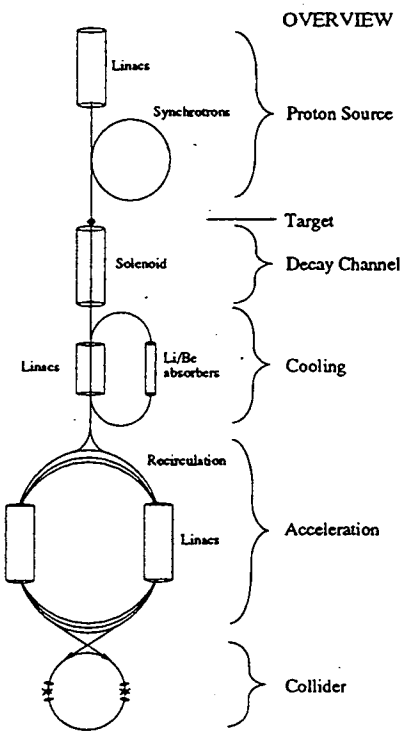

Figure 1: Schematic of the $\mu^+\mu^-$ Collider Complex.

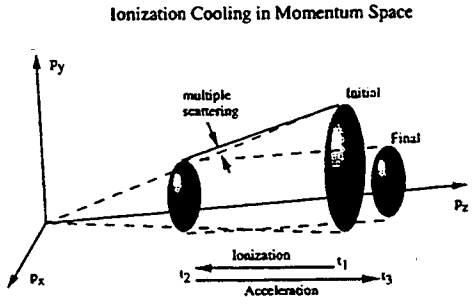

Figure 2: Basic principle of ionization cooling of transverse emittance.

LBNL-38938
UC-414

RF Power Source Development at the RTA Test Facility

D. Anderson, S. Chattopadhyay, S. Eylon,
E. Henestroza, L. Reginato, A. Sessler,
D. Vanecek, S. Yu, T. Houck, G. Westenskow,
S. Lidia, and G. Giordano
Accelerator and Fusion Research Division

June 1996
Presented at the
European Particle Accelerator Conference,
Barcelona, Spain,
June 10–14, 1996,
and to be published in
the Proceedings

RF POWER SOURCE DEVELOPMENT AT THE RTA TEST FACILITY*

D. Anderson, S. Chattopadhyay, S. Eylon, E. Henestroza, L. Reginato, A. Sessler, D. Vanecek, S. Yu, Lawrence Berkeley National Laboratory; T. Houck, G. Westenskow, Lawrence Livermore National Laboratory; S. Lidia, Univ. of California (Davis); G. Giordano, Univ. of Milano

Abstract

The RTA Test Facility has been established at LBNL to demonstrate key concepts related to both physics and technical issues of a proposed two-beam accelerator 1.5-TeV c.m. upgrade of the NLC collider design (TBNLC). A prototype two-beam accelerator rf power source will be constructed at the RTA Test Facility which will allow testing of the major components of the TBNLC rf power source. The proposed test facility and its current status are described. Performance of the induction accelerator pulsed power system, including the induction cores, is a key issue affecting both cost and efficiency of the rf power source. Recent test results on the RTA pulsed power system are presented.

1 INTRODUCTION

For several years a Lawrence Berkeley National Laboratory (LBNL) and Lawrence Livermore National Laboratory (LLNL) collaboration has studied rf power sources based on the RK-TBA concept [1]. This effort has included both experiments [2] and theoretical studies [3]. Last year, a preliminary design study for a rf power source suitable for the NLC was published [4]. The design specifically addressed issues related to cost, efficiency, and technical issues. For a 1-TeV center of mass energy design, the rf power source is comprised of 50 subunits, each about 340 m in length with 150 extraction structures generating 360 MW per structure. Estimated conversion efficiency of wall plug energy to rf energy for this source could be > 40%. Theory/simulations showed acceptable drive beam stability through the relativistic klystron, and no insurmountable technological issues were uncovered.

We have established a test facility at LBNL to verify the analysis used in the design study. The principle effort is constructing a TBNLC rf power source prototype, called the RTA [5]. All major components of the TBNLC rf power source will be tested. However, due to fiscal constraints, the RTA will have 8 rf extraction structures, with a possible upgrade to 12. See Fig 1. Table 1 is a comparison between the pertinent parameters for TBNLC and the RTA. The pulsed power system and induction cells in the extraction section will be similar for both machines, allowing a demonstration of efficiency and establishing a basis for costing. Other features shared between the two machines include transverse chopping for initial beam modulation, adiabatic compression to increase the rf current while accelerating the beam, PPM quadrupole focusing, and detuned rf extraction structures.

Issues to be addressed by the RTA are drive beam dynamics, efficiency, emittance preservation and rf power quality. Efficiency can be separated into the conversion efficiency of wall plug power into beam power and beam power into rf power. The conversion of wall plug power into beam power can be fully measured in the RTA. High conversion efficiency of beam to rf power is only realized in a system with many extraction structures. For TBNLC, the number of extraction structures is limited by beam stability and transport issues. The direct study of beam dynamics involving transport over many tens of extraction structures will not be possible with the RTA. The reduced beam energy in the RTA extraction section does allow the observation of almost an entire synchrotron period. This should be sufficient for the beam to approach a steady state condition that can be extrapolated to a full scale system. Verification of simulations used to model beam dynamics in RK-TBA's is a high priority. Beam dynamics issues such as focusing magnet misalignments, transverse modulation, and adiabatic compression can be studied.

TABLE 1. Comparison between RTA and the TBNLC.

Parameter	RTA	TBNLC
Pulse Duration	200 ns	300 ns
Rise Time	100 ns	100 ns
Current		
Pre-Modulation	1.2 kA	1.2 kA
Extraction Section	600 A dc 1.1 kA rf	600 A dc 1.1 kA rf
Beam Energy		
Injector	1 MeV	1 MeV
Modulator	2.8 MeV	2.5 MeV
Extraction	4.0 MeV	10.0 MeV
Bunch Compression	240° - 110°	240° - 70°
Extraction Section PPM Quadrupoles		
Betatron Period	1 m	2 m
Lattice Period	20 cm	33.3 cm
Phase Advance	72°	60°
Occupancy	0.5	0.48
Pole Tip Field	870 G	812 G
Beam Diameter	8 mm	4 mm
RF Power		
Frequency	11.4 GHz	11.4 GHz
Power/Structure	180 MW	360 MW
Structures	Standing & Traveling-Wave	3 cell Traveling-Wave
Output Spacing	1 m	2 m

2 PULSED POWER SYSTEM

Conversion of wall plug power into induction drive beam power is a significant factor in the rf power source efficiency. The efficiency of a TBA induction accelerator depends on several factors. Beam transport dynamics will determine the size of the beam pipe. The rf power requirement determines the pulse duration, beam current,

*The work was performed under the auspices of the U.S. Department of Energy by LLNL under Contract W-7405-ENG-48 and by LBNL under Contract DE-AC03-76SF00098

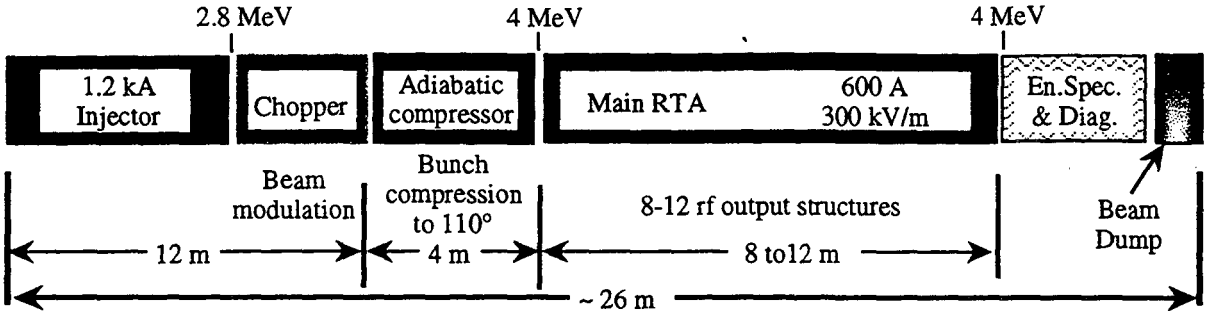

FIGURE 1. Schematic of the proposed RTA showing major components.

accelerating gradient, and repetition rate. Once these factors are established, the outer radius and material of the core can be calculated from: $\Delta V\ \Delta t = \Delta B\ A\ F_p$, where ΔV is cell voltage swing, Δt is pulse duration, ΔB is core flux swing, A is core cross section, and F_p is core material packing factor. The core volume increases nearly as the radius squared, so smaller, more efficient and lower cost induction cells can normally be obtained by using higher ΔB materials and minimizing the inner radius.

Several core materials have been tested at the RTA Test Facility [6]. Two METGLAS® alloys, 2605SC and 2714AS, have been selected for use in the RTA. The alloy 2605SC has a ΔB of ~ 2.5 T with a core loss of ~ 2 kJ/m^3 for a 400 ns pulse and 20 μm thick ribbon. The alloy 2714AS has a lower ΔB, ~ 1.1 T, but a much lower core loss of ~ 150 J/m^3 with 18 μm ribbon. It is important that core tests are performed with the expected pulse shape and duration for accurate loss measurements. For our TBNLC geometry, the low core loss 2714AS can achieve a conversion efficiency of wall plug power to drive beam power of 59%, a substantial improvement over 2605SC.

The modest repetition rate (120 Hz) and current rise time (100 ns) envisioned for the NLC permit the use of a simple, and cost effective thyratron driven modulator. The total induction cell core is segmented longitudinally into smaller cores each individually driven at 20 kV or less. Driving at this voltage level avoids a separate step-up transformer. Length of the induction cell, thus number of cores per cell, is set by geometrical constraints due to extraction structures, magnet positions, etc. The TBNLC design in Fig 3 has 5 cores per cell while the RTA has 3.

Beam energy flatness is an important issue affecting beam transport and rf phase variation. The current drive to the cores is nonlinear for a constant amplitude voltage pulse since the core saturates outward from the inner radius. This effect is shown in Fig 4 where the voltage pulse has ~ 200 ns of flat top during which the current increases non-linearly. The generated voltage amplitude can be kept constant, within bounds, during the initial stages of core saturation by tapering the impedance of the PFN stages. Our PFN will consist of many coupled L-C stages. Lower aspect ratio ($\Delta r/\Delta z$) cores saturate more uniformly, thus requiring less impedance tapering.

3 INJECTOR

The injector consists of two sections, a 1-MV, 1.2 kA induction electron source, referred to as the gun, followed by several induction accelerator cells to boost the energy to 2.8 MeV. Two goals of the design are minimizing

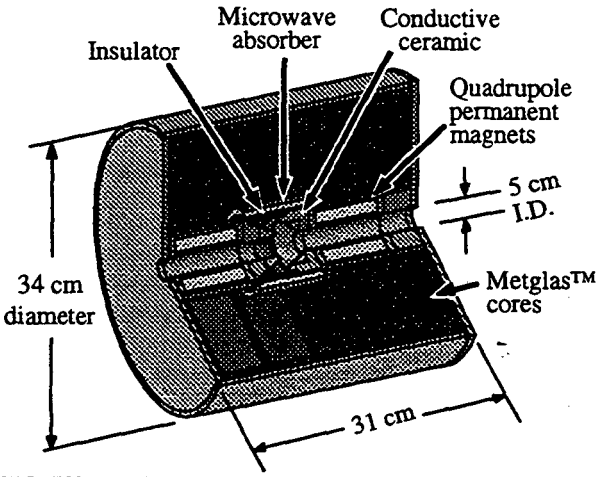

FIGURE 3. A proposed RK-TBA induction cell design illustrating longitudinal core segmentation.

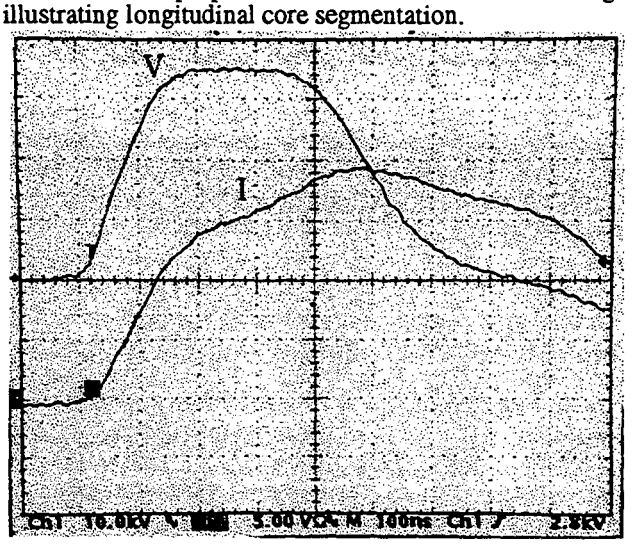

FIGURE 4. Oscilloscope traces of pulsed power system test on a mockup induction cell for the RTA gun. Time scale: 100 ns/div. V is cell voltage (1 kV/div), I is PFN current (50 A/div).

electrical field stresses in the gun and realizing the lowest possible emittance growth. Gun induction cores are segmented radially to reduce the individual aspect ratios with each driven separately at about 14 kV. Components of the induction cells for the gun are in fabrication.

A novel feature of the gun design is the insulator, a single, 30 cm ID, PYREX® tube with no intermediate electrodes. Average gradient along the insulator at the operating voltage of 500 kV is ~ 5.1 kV/cm. Maximum fields at the triple points, intersection of insulator, vacuum, and metal, are less than 3.5 kV/cm. Maximum

surface fields in the cathode half of the gun are about 85 kV/cm. The rational for using PYREX® is to explore cost reduction methods for induction injectors. PYREX® is less expensive than ceramic, and additional savings are realized by avoiding intermediate electrodes. Our design allows for the addition of intermediate electrodes and/or substitution of a ceramic insulator to minimize the increased risk associated with this approach.

The focusing solenoidal field profile must be optimized for the injector to control the beam radius while minimizing emittance growth. A new electrode package and larger dispenser cathode will likely be required for the desired low-emittance 1.2-kA, 1-MeV electron beam. The design goal is for beam radius < 5 mm and horizontal normalized edge emittance < 250 π-mm-mr at the end of the injector. Alignment of the solenoids is critical to avoid corkscrew motion and emittance growth. Incorporating homogenizer rings [7] with the solenoids could reduce the need for correction coils and simplify alignment.

Experience operating other induction accelerators has shown that careful alignment of the solenoids may not be sufficient to reduce the amplitude of the corkscrew motion [8] to the 0.5 mm desired for the RTA injector. We plan to use a time independent steering algorithm [9] developed at LLNL to control steering coils on the solenoids. The algorithm corrects for the Fourier component at the cyclotron wavelength of the field error.

4 BEAM DYNAMICS ISSUES

Beam dynamics issues related to longitudinal and transverse stability, modulation, and transport have been presented in detail elsewhere [3, 4, 10, 11]. A brief description of these issues is given here. Initial beam modulation is accomplished with a transverse chopping technique. After this modulator section, an adiabatic compressor, a system of idler cavities and induction accelerator modules, is used to bunch the beam and further accelerate it to an average energy of 4 MeV. The lower frequency component of the transverse beam breakup instability is controlled by Landau damping. Control of the higher frequency component, excited in the rf cavities, is accomplished with the focusing system in a technique that we refer to as the "Betatron Node" scheme. The rf extraction structures are appropriately detuned to compensate for space charge and energy spread effects so that the longitudinal current distribution is stable.

5 RF POWER EXTRACTION

After the adiabatic compressor, the beam enters the extraction section. where beam energy is periodically converted into rf energy (via extraction cavities) and restored to its initial value (via induction modules). Both traveling wave (TW) and standing wave (SW) structures are being considered for the extraction section of the RTA. The TBNLC design uses TW structures to reduce the surface fields associated with generating 360 MW per structure. RTA is designed to generate 180 MW per structure. Thus, inductively detuned SW cavities are a practical alternative. An interesting design variation is based on Shintake's choke mode cavity [12].

6 SUMMARY

Construction has started on the RTA, a prototype rf power source based on the RK-TBA concept. Testing of material for the induction cores is completed and two METGLAS® alloys selected. The pulsed power system for the gun is based on driving individual cores at ~ 14 kV using glass thyratron tubes switched at 28 kV. The pulsed power system design for later portions of the RTA will continue to develop during testing of the gun. A novel feature of the gun is the use of PYREX® tubes as 500 kV insulators. Satisfactory performance of these insulators would demonstrate an inexpensive alternative to the more standard graded, ceramic insulator.

The RTA will be used to study physics, engineering, and costing issues involved in the application of the RK-TBA concept to linear colliders. All major components of a rf power source suitable for the NLC can be studied, e.g. the pulsed power system, current modulating system, ppm quadrupole focusing, and detuned rf extraction cavities. Some of the more important issues that will be address are efficiency, longitudinal beam dynamics, beam stability, emittance preservation, and rf power quality.

7 REFERENCES

[1] Sessler, A.M. and Yu, S.S., *Phys. Rev. Lett.* **54**, 889 (1987).

[2] Westenskow, G.A., and Houck, T.L., *IEEE Trans. on Plasma Sci.*, **22**, 750 (1994).

[3] Giordano, G., et al., "Beam Dynamic Issues in an Extended Relativistic Klystron," *Proc. 1995 IEEE Particle Accelerator Conf.*, p. 740.

[4] Yu, S.S., et al., "RK-TBA Based Power Source for a 1-TeV NLC," LBID-2085, Lawrence Berkeley National Laboratory, Feb. 1995.

[5] Houck, T.L., and Westenskow, G.A., "Prototype Microwave Source for a Relativistic Klystron Two-Beam Accelerator" to be published in *IEEE Trans. on Plasma Sci.*, Special Issue on High Power Microwave Generators.

[6] Reginato, L., et al., "Engineering Conceptual Design of the Relativistic Klystron Two-Beam Accelerator Based Power Source for 1-TeV NLC," *Proc. 1995 IEEE Particle Accelerator Conf.*, p. 743.

[7] Feinberg, B., et al., *Nucl. Instr. and Meth.*, **203**, pp. 81–85 (1982).

[8] Allen, S.L., et al., "Measurements of Reduced Corkscrew Motion on the ETA-II Linear Induction Accelerator," *Proc. 1991 IEEE Particle Accelerator Conf.*, pp. 3094-3096.

[9] Chen, Y-J, *Nucl. Instr. and Meth.*, **A292**, pp. 455–464 (1990).

[10] Haimson, J. and Mecklenburg, B., "Design and Construction of a Chopper Driven 11.4 GHz Traveling Wave RF Generator," *Proc. 1989 IEEE Particle Accelerator Conf.*, 89CH2669, pp. 243-245

[11] T.L. Houck, et al., "RK-TBA Prototype RF Source," *Proc. 1996 Pulsed RF Sources for Linear Colliders Workshop*.

[12] Shintake, T., "The Choke Mode Cavity," *Jpn. J. Appl. Phys.* **31**, pp. L1567–L1570, 1992.

LBNL-38937
UC-414

Sensitivity Studies of Crystalline Beams

J.Wei and A.M. Sessler
Accelerator and Fusion Research Division

June 1996
Presented at the
European Particle Accelerator Conference,
Barcelona, Spain,
June 10–14, 1996,
and to be published in
the Proceedings

SENSITIVITY STUDIES OF CRYSTALLINE BEAMS*

Jie Wei, Brookhaven National Laboratory, Upton, New York 11973, U.S.A.
Andrew M. Sessler, Lawrence Berkeley Laboratory, Berkeley, California 94720, U.S.A.

Abstract

The equations of motion are presented, appropriate to interacting charged particles of diverse charge and mass, subject to the external forces produced by various kinds of magnetic fields and radio-frequency (rf) electric fields in storage rings. These equations have been employed in the molecular dynamics simulations for sensitivity studies of crystalline beams. The two necessary conditions for the formation and maintenance of crystalline beams are summarized. The effects of lattice shear and AG focusing, magnetic field imperfection, and ion neutralization on crystalline beam heating is presented.

1 INTRODUCTION

In previous work, the nature of crystalline beams has been studied by many investigators.[1]In particular, we have made a systematic study in a series of papers[2] which has consisted of deriving the equations of motion for charged particles undergoing Coulomb interaction in a real storage ring, and then using them to explore many properties of crystalline beams.

In this paper, we carry on our investigation with sensitivity studies of crystalline beams. We summarize first in Section 2 the generalized equations of motion, and then in Section 3 the conditions for the formation and maintenance of crystalline beams. In Sections 4, 5, and 6, we present the results of sensitivity studies of crystalline beams on lattice shear and AG focusing, lattice imperfection, and ion neutralization. The conclusions are given in Section 7.

2 EQUATIONS OF MOTION

In order to adopt the molecular dynamics (MD) methods, we employ[2] a rotating frame (x, y, z, t) of a reference particle in which the orientation of the axes is rotating so that the axes are constantly aligned to the radial (x), vertical (y), and tangential (z) direction of motion. It is convenient to define a reference particle with charge state Z_0 and atomic mass M_0. We scale dimensions in terms of the characteristic distance ξ, with $\xi^3 = r_0\rho^2/\beta^2\gamma^2$, where $r_0 = Z_0^2e^2/M_0c^2$, the velocity of the reference particle is βc, its energy is γM_0c^2, and it moves on an orbit with bending radius ρ in magnetic field B_0. We measure time in units of $\rho/\beta\gamma c$ and energy in units of $\beta^2\gamma^2 Z_0^2e^2/\xi$. For the ith species of ions with charge state Z_i and mass M_i, we define the relative charge and mass with respect to the reference values

$$\bar{Z}_i \equiv Z_i/Z_0, \quad \text{and} \quad m_i \equiv M_i/M_0. \tag{1}$$

In a bending region with bending radius ρ, the Hamiltonian for particles of the ith species is derived as

$$H_i = \frac{1}{2}\left(P_x^2 + P_y^2 + P_z^2\right) + \frac{1}{2}\left[x^2 + \left(\frac{\bar{Z}_i}{m_i} - 1\right)\gamma^2 z^2\right] - \left(2 - \frac{\bar{Z}_i}{m_i}\right)\gamma x P_z + \left(\frac{\bar{Z}_i}{m_i} - 1\right)\frac{\rho}{\xi}\, x + V_{Ci}, \tag{2}$$

where the Coulomb potential is

$$V_{Ci} = \sum_j \frac{\bar{Z}_i\bar{Z}_j}{m_i\sqrt{(x_j - x)^2 + (y_j - y)^2 + (z_j - z)^2}}, \tag{3}$$

and the summation, j, is over all the other particles. In a straight section, where there is no bending of particles, there often are quadrupole magnets for focusing, sextupole magnets for chromatic correction, and electric field for acceleration or bunching, etc.. If the normal quadrupole, skew quadrupole, and sextupole strengths are represented by

$$n_1 = -\frac{\rho}{B_0}\frac{\partial B_y}{\partial x}, \quad n_{1s} = -\frac{\rho}{B_0}\frac{\partial B_y}{\partial y}, \quad n_2 = -\frac{\rho}{B_0}\frac{\partial^2 B_y}{\partial x^2}, \tag{4}$$

respectively, the Hamiltonian can be derived as

$$H_i = \frac{1}{2}\left(P_x^2 + P_y^2 + P_z^2\right) - \frac{n_1}{2}\frac{\bar{Z}_i}{m_i}(x^2 - y^2) - n_{1s}\frac{\bar{Z}_i}{m_i}xy - \frac{n_2\xi}{6}\frac{\bar{Z}_i}{m_i}(x^3 - 3xy^2) + V_{Ci} + U_s, \tag{5}$$

where the electrical force F_s in the reduced units can be expressed in terms of electric field E_s measured in the laboratory frame,

$$F_s \equiv -\frac{\partial U_s}{\partial z} = \frac{\bar{Z}_i}{m_i}\frac{Z_0eE_s\xi}{M_0c^2}\left(\frac{\rho}{\xi\beta\gamma}\right)^2. \tag{6}$$

The equations of motion can be obtained from the Hamilton's equations using Eqs. 2 and 5.

3 CONDITIONS FOR CRYSTALLIZATION

The first condition arises from the criteria of stable transverse motion when particles are crystallized. It

* Work supported by the DOE, Office of Energy Research, Office of High Energy and Nuclear Physics, under Contract No.DE-AC03-76SF00098 and DE-AC02-76CH300016.

requires that the ring is AG focusing, and that the energy of the particles is less than the transition energy of the ring.

The second condition arises from the criteria that there is no linear resonance between the phonon modes of the crystalline structure and the machine lattice periodicity. It requires that the ring is designed such that the lattice periodicity is at least $2\sqrt{2}$ as high as the maximum betatron tune to adequately maintain crystalline beams at any beam density.

4 EFFECTS OF LATTICE SHEAR AND AG FOCUSING

According to the first condition, a storage ring for crystalline beams is necessarily AG focusing. In addition to bending sections, the ring also consists of straight sections for cooling, acceleration, and experiments. As the crystalline beam circulates around the ring, its ground state is periodic in time with the period of the ring lattice. Fig. 1 shows an example of the

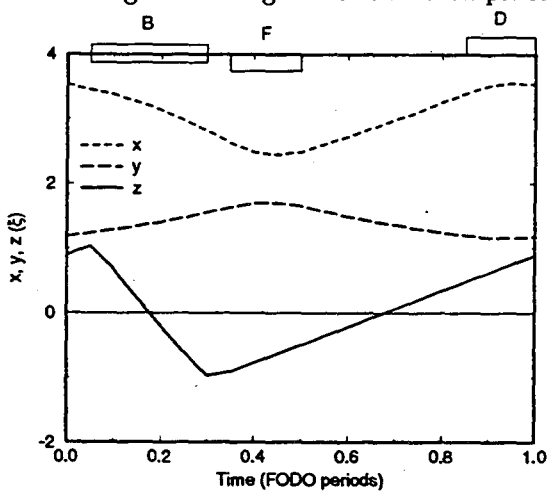

Figure 1: Typical trajectory of a coasting crystalline beam. Lattice components are displayed on the figure: B is a bending section, F and D are focusing and defocusing sections.

ground state of a crystalline beam. The ground state structure is a single-layer shell. The machine, having a periodicity of 10, consists of 10 FODO cells with 25% bending with $\nu_x = 1.96$, $\nu_y = 2.06$, and $\gamma_T = 1.81$. The beam energy corresponds to $\gamma = 1.4$. The variation in time of the trajectory in the transverse direction (x and y) corresponds to AG focusing, and the variation in the longitudinal direction (z) corresponds to the variation in bending and straight sections (shear).

Because of the time dependence, the crystalline structure absorbs energy from the lattice at non-zero temperature. Define the normalized temperature[2] in terms of the deviation of momenta P_x, P_y and P_z from their ground-state values, squared and averaged over particles for a relatively long time. The + symbol in Fig. 2 shows the heating rate as a function of temperature for a beam at density $N/L = 5$ (5 particles per unit MD cell). In order to investigate the effects of AG focusing and shear on the heating rate, we created two idealized machine lattices with the same transverse tunes and lattice periodicity for comparison: one with the similar AG focusing but constant bending around the ring (as shown by the filled squares in Fig. 2); the other with the same 25% bending section but constant focusing around the ring (as shown by the empty squares in Fig. 2). In all the cases, the phonon spectrum of the beam is similar relative to the lattice modulation frequency (periodicity). Consequently, the heating behavior is similar, i.e., AG focusing and shear cause similar beam heat up. Not surprisingly, when the bending and focusing are both constant with time, the temperature of the crystalline beam stays constant.

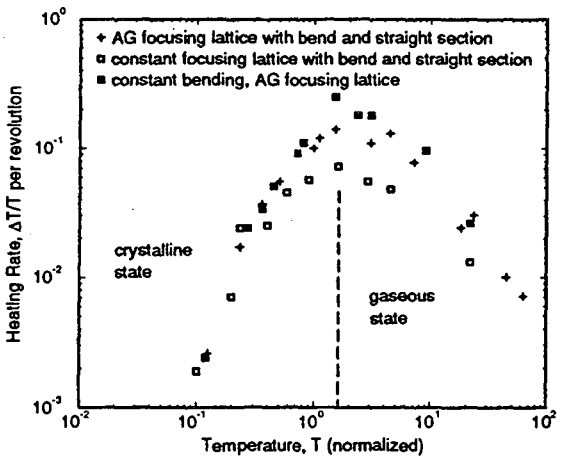

Figure 2: Heating rates as functions of the normalized temperature for crystalline beams of equivalent density but different machine lattices.

5 EFFECTS OF MAGNETIC FIELD IMPERFECTION

In an actual magnet in a storage ring, the fields will differ somewhat from the ideal design, resulting in beam misalignment and focusing gradient errors. Strictly speaking, the machine lattice periodicity is equal to 1, and the second condition for crystallization is not satisfied. In Section 4, we have demonstrated that the effect of variation in bending and focusing on beam heating is similar. Therefore, we here only present the results on the effects of field gradient error in the quadrupole magnets.

With the same machine lattice as in Fig. 1, the + symbol in Fig. 3 shows the heating rate as a function of normalized temperature T for the beam at density $N/L = 5$. With $Z = A = 1$, and $\xi = 1.2$ μm, the conventionally used beam temperature T_B can be obtained from T by $T_B \approx 7.5\ T$ [°K]. To study the effect of gradient errors, we assume that the strength n_{Fi} and

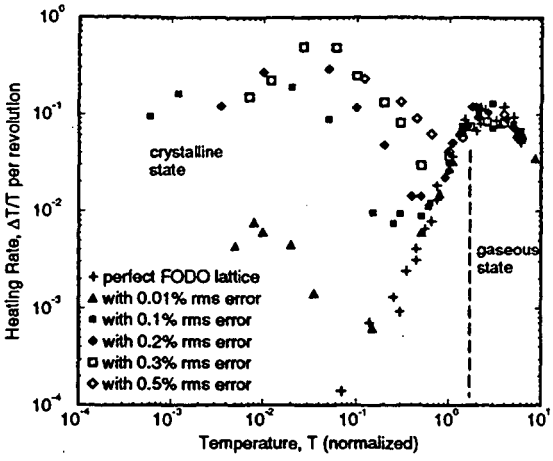

Figure 3: Effects of gradient errors in storage ring quadrupole magnets for a beam of density $N/L = 5$ ($N = 100$, and $L = 20\,\xi$).

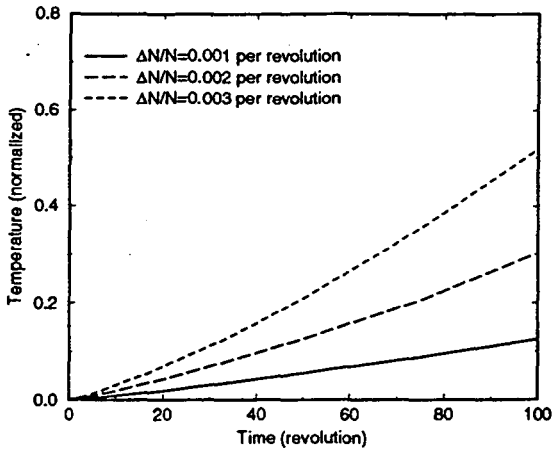

Figure 4: Temperature evolution for ion neutralization rate of $\Delta N/N = 0.001, 0.002$, and 0.003 per revolution in the absence of cooling, starting from the crystalline beam ground state at density $N/L = 5$.

n_{Di} of the ith focusing and de-focusing quadrupoles randomly deviate from their design values ($n_F = -1.4$ and $n_D = 2.35$ at $\rho = 1$ m) according to the expression

$$n_{Fi,Di} = n_{F,D}\,(1 + g\,G_i)\,, \qquad (7)$$

where g is the amplitude of the random error, and G_i returns a normally distributed deviate with zero mean and unit variance. Fig. 3 shows the change in heating rate when g is increased from 0 to 10^{-4}, 10^{-3}, 2×10^{-3}, 3×10^{-3}, and 5×10^{-3}. As the error increases, the lattice deviates significantly from its design periodicity of 10. Even at low temperature, the beam absorbs energy from the imperfect lattice. Fig. 3 indicates that when the rms error is larger than 10^{-3}, the heating rate at low temperature exceeds the peak rate at $T \approx 2$. On the other hand, the accuracy in the construction of modern storage ring magnets is typically at 10^{-4} level. With this standard, magnetic imperfection is of little concern in crystalline beam maintenance.

6 EFFECTS OF ION NEUTRALIZATION

Ion neutralization caused by gas scattering and other mechanisms can disrupt the crystalline structure and cause beam heating. We simulate this neutralization process by removing the particles from the crystalline structure at a given rate. Starting from the ground state, when a particle is removed, the structure deviates from its ground state. The potential energy is then transferred into kinetic energy, resulting in a finite temperature. With the same lattice as in Fig. 1 and the same beam density of $N/L = 5$, Fig. 4 shows the increase of heating rate for various neutralization rates of 0.1%, 0.2%, 0.3% per revolution. It is found that the peak rate ($T \approx 2$ in Fig. 3) from the lattice heating corresponds to a neutralization rates of about 0.5% per revolution. Therefore, ion neutralization at a rate much less than $\Delta N/N$ =0.5% per revolution is of little concern in crystalline beam formation.

7 CONCLUSIONS

In this paper, we have summarized the conditions for the formation and maintenance of crystalline beams. We have demonstrated that lattice shear and AG focusing have similar effects in beam heating. In an example, we have shown that magnetic field error at less than 0.1% level can be tolerated. Ion neutralization at a rate much less than 0.5% per revolution is also of little concern in crystalline beam formation.

Acknowledgment The MD code used to generate results in this paper was originally written by X-P. Li.

8 REFERENCES

[1] For example, N.S. Dikanskiĭ and D.V. Pestrikov, Proc. of the Workshop on Electron Cooling and Related Applications, KfK 3846, ed. H. Poth, (1984); J.P. Schiffer and P. Kienle, Z. Phys. A **321**, 181 (1985); J.P. Schiffer and O. Poulsen, Europhys. Lett. **1**, 55 (1986); A. Rahman and J.P. Schiffer, Phys. Rev. Lett. **57**, 1133 (1986).

[2] J. Wei, X-P Li, and A.M. Sessler, Report BNL-52381, Upton (1993); J. Wei, X-P Li, and A.M. Sessler, Proc. 1993 Part. Accel. Confe., Washington, D.C., 1993, p. 3527; J. Wei, X-P Li, and A.M. Sessler, Proc. Workshop on Beam Cooling and Related Topics, Montreux, 1993, p. 366; J. Wei, X-P Li, and A.M. Sessler, Phys. Rev. Lett. **73**, 3089 (1994); J. Wei, X-P Li, and A.M. Sessler, Adv. Accel. Concepts, Fontana, AIP Confe. Proc. **335**, p.224 (1995); J. Wei, X-P Li, and A.M. Sessler, Proc. 1995 Part. Accel. Confe., Dallas, p.2946 (1995); X-P Li, A.M. Sessler, and J. Wei, Proc. 1994 Euro. Part. Accel. Confe., London, 1379 (1994); J. Wei, A.Draeseke, A.M. Sessler, and X-P. Li, Proc. 31st Workshop of the INFN Eloisatron Project on Crystalline Beams and Related Issues, Erice, Italy, 1995 (to be published).

LBNL-38936
UC-414

Single Bunch Collective Effects in Muon Colliders

W.-H. Cheng, A.M. Sessler, J.S. Wurtele,
and K.Y. Ng
Accelerator and Fusion Research Division

June 1996
Presented at the
European Particle Accelerator Conference,
Barcelona, Spain,
June 10–14, 1996,
and to be published in
the Proceedings

SINGLE BUNCH COLLECTIVE EFFECTS IN MUON COLLIDERS *

Wen-Hao Cheng, Andrew M. Sessler, Jonathan S. Wurtele
Lawrence Berkeley Laboratory
Berkeley, California 94720
and
King Yuen Ng
Fermilab, P.O. Box 500, Batavia, IL 60510

Abstract

Theoretical examination is made of single bunch collective effects in the collider ring of a 2 Tev × 2 Tev Mu-Mu Collider complex. The situation involves an intense bunch, a short bunch, a small momentum compaction, a rather large impedance for the rf system, and luminosity life time limited by muon decay to of the order a thousand turns. The use in rings of techniques such as BNS damping, developed for linear colliders, is discussed. Qualitative descriptions and numerical simulation results are presented.

1 INTRODUCTION

The design of a high luminosity ($2.5 \times 10^{30}\text{cm}^{-2}$ per collision) muon collider ring, from the perspective of the physics of collective effects, has some unique features which need to be examined. (1) The bunch has a large charge: $N = 2\times10^{12}$. (2) The bunch is short: $\sigma_z = 3\,\text{mm}$. (3) The momentum compaction α is very small: $\alpha \leq 10^{-6}$. (4) Muons have a very short life time: $\tau_\mu \simeq 41.6$ ms at 2 Tev, corresponding to a thousand "effective" turns in a ring with the circumference of 7 kilometers.

These features lead us to some unusual aspects of the ring operation: the intense bunch required for the high luminosity makes instabilities likely and very small α requires careful estimations of nonlinear corrections to the particle orbit and to the collective dynamics.

The longitudinal equation of motion of a particle traveling in a circular machine can be written as

$$z' = -\eta\delta, \quad \delta' = K(z), \tag{1}$$

where z is the oscillation amplitude with respect to the bunch center, $' = d/ds$, s measures distance around the ring, $\delta = dp/p$, $\eta = \alpha - 1/\gamma^2$, $\alpha = pdC/Cdp$. The force $K(z)$ that a particle experiences can be modeled as having two parts, one is due to the radio frequency (rf) cavities, and the other is from the wake fields generated by the interaction between beam and cavities or other components of its electromagnetic environment,

$$K(z) = K_{rf}(z) + K_{wake}(z), \tag{2}$$

where

$$K_{rf}(z) = eV_{rf}(z)/CE, \tag{3}$$

and

$$K_{wake}(z) = -(r_0/\gamma C)\int_z^\infty dz'\rho(z')W_0'(z-z'). \tag{4}$$

In Eq. (4), $T_0 = 2\pi/\omega_0 = C/c$, $E = \gamma m_\mu c^2$, $r_0 = e^2/m_\mu c^2$, $N = \int dz'\rho(z')$, and $C = 2\pi R$ is the circumference of the collider ring.

In Eq. (3), when the amplitude of synchrotron motion is small compared with the rf wavelength such that the rf voltage is linearized as $V_{rf}(z) = \hat{V}\sin(\omega_{rf}z/c) \approx \hat{V}\omega_{rf}z/c$ and the momemtum compaction is expanded as $\eta = \eta_1 + \eta_2\delta + \eta_3\delta^2$ (with the contributions from η_2 and η_3 negligible), the synchrotron oscillation frequency is $\omega_{s0} = (e\eta_1 c\omega_{rf}\hat{V}/CE)^{1/2}$.

The transverse equation of motion is

$$y''(z,s) + (\omega_\beta^2/c^2)\,y(z,s) = -(r_0/\gamma C)\int_z^\infty dz'\rho(z')W_1(z-z')y(z',s). \tag{5}$$

In this paper, we discuss several single bunch collective effects, and illustrate the impacts and the cures of collective instabilities for the muon collider. Some important simulation results are presented.

2 STATIC EFFECTS

As a starting point we consider a TESLA-like rf system, and a quasi-isochronous lattice which has $\eta_1 = 10^{-6}$, with the contributions from η_2 and η_3 negligible. With a bunch length $\sigma_z = 3$ mm, $\sigma_\delta = 1.5\times10^{-3}$ rms energy spread and an 130MV of L-band rf, the muon bunch is matched to the rf and a muon would undergo $\sim .56$ synchrotron oscillations in one thousand turns.

2.1 Parastic Loss

The beam loses energy when it experiences the impedance of the rf cavities. We model the rf impedance by using Perry Wilson's scaling formula for the longitudinal wake function [1]. Explicitly, the wake function for the TESLA's rf frequency, $W_0'(z<0) = 226(f_{TESLA}/f_{SLAC})^2 \times \exp[-(-zf_{TESLA}/0.1839f_{SLAC})^{0.605}]$, where $f_{TESLA} = 1.3$GHz and $f_{SLAC} = 2.856$GHz.

* Work supported by the U.S. Department of Energy under contract No. EDDEFG-03-95ER-40936, DE-AC03-76SF00098 and DE-AC02-76CHO3000

Casuality requires: $W_0'(z) = 0$ if $z > 0$. Our simulation code computes the wake voltage $V_{wake}(z) = \int_z^\infty dz' \rho(z') W_0'(z - z')$; and the energy loss $\Delta\mathcal{E} = -\int_{-\infty}^{\infty} dz \int_{-\infty}^{\infty} dz' \rho(z') W_0'(z - z')$.

The peak wake voltage is further scaled from Wilson's formula to give 17V/pC/m at $1\sigma_z$ for a Gaussian beam. This choice of wake amplitude makes it consistent with the TESLA rf cavity studies [2]. The beam-loading factor, defined as $\Delta\mathcal{E}$/particle/V_{rf}, is 10% when only the cavity losses are included. The energy loss due to the resistive-wall are estimated to roughly equal the rf losses [3], but have not been explicitly included in our calculation. Other losses have not been calculated, and may lead to an increase in the rf voltage. These losses will need to be replenished even if the momentum compaction is reduced to $\eta_1 = 10^{-7}$, as may be required because of microwave instabilities.

2.2 *Potential Well Distortion*

The effects of radiation and diffusion of muons are small in a muon lifetime (radiation damping time $\sim 10^6$ turns), so that, unlike in electron rings, equilibrium is not achieved by radiation damping. The intense muon bunch generates significant wakes, and these wakes in turn cause significant changes in the rf potential. This potential-well distortion causes oscillation of the bunch center, bunch size, and distribution function in the rf bucket. Fig. (1) shows the oscillations of the rms bunch size and bunch energy spread. The bunch centroid tends to move forward to a higher rf voltage, so that the energy loss can be compensated. As a result, it makes a counter-clockwise rotation in $\delta - z$ phase space, as shown in Fig. (2). The parasitic losses and the bunch centroid shift are compensated for by injecting the beam with an rf phase offset of 0.082 radians with respect to the bunch center, as shown by the dashed line in Fig. (2).

3 COHERENT EFFECTS

3.1 *Microwave Instability*

The longitudinal microwave instability is presently considered the most serious challenge to maintaining a short bunch. Presently studies are underway to examine the limits this instability places upon Z/n. The ring parameters obviously will not satisfy the Keil-Schnell criterion for stability, but rather we hope to reduce the growth rate to an acceptable amount during the 1000 turns of beam storage. Specifically, the growth rate and the damping rate of the longitudinal microwave instability of a short bunch is [4]

$$\tau_{growth}^{-1} = n\omega_0 \sqrt{\frac{\eta I_p Z_0^{\parallel}/n}{2\pi E/e}}, \quad \tau_{damping}^{-1} = n\omega_0 \eta \sigma_\delta, \quad (6)$$

where $n = \omega/\omega_0$. If $\eta = 10^{-6}$ and $Z/n \simeq 1\Omega$, then for the ring parameters, $\tau_{growth}^{-1} \simeq 8.7n \times 10^{-3} s^{-1}$ and $\tau_{damping}^{-1} \simeq 0.4n \times 10^{-3} s^{-1}$. The instability growth rate is much faster than the damping rate.

The microwave instability growth rate is weaker at smaller η values, and the instability may require the lattice to operate at $\eta = 10^{-7}$. At this value of η the particles barely move longitudinally, and the possibility and consequences of compensating for the wake potential with rf are being considered. In the absence of significant longitudinal motion the main problem is to maintain an energy spread within the longitudinal acceptance of the ring.

3.2 *Beam-Break-Up*

For times much shorter than the synchrotron oscillation period, particles are almost frozen longitudinally in the bunch, and the transverse wakefield dynamics has many similarities with that in a linac [5]. In a linac, the transverse wake field generated by the head of the bunch drives the tail, causing Beam-Break-Up (BBU). A dimensionless parameter that characterizes the BBU strength is [6]

$$\Upsilon(z) = Nr_0 |\langle W_1(z) \rangle| c/4\omega_\beta \gamma, \quad (7)$$

where ω_β is the betatron angular frequency, and $\langle W_1(z) \rangle = \int_z^\infty dz' W_1(z - z') \rho(z')$ is the convoluted total transverse wake function. The tail of an off-axis bunch doubles its offset in a number of turns $n \simeq 1/\Upsilon$, so long as $n \ll 1/2\nu_s$, i.e., when the particle's synchrotron motion can be ignored. Here ν_s is the synchrotron tune.

Simulation results for the BBU-like instability using a resonator model are shown in Fig. (3). The main point is that while the motion is unstable, it is easily cured with only a small amount of BNS damping, as discussed below.

3.3 *Head-Tail Instabilities*

When the transverse oscillation frequency is modulated by the energy oscillation, the chromaticity, which is the slope of the frequency to the energy, builds up a head-tail phase that bootstraps from the first half synchrotron period to the next, and drives the system into instability without threshold. This head-tail instabilities occurs in both transverse and longitudinal motions [7]. The effect of transverse head-tail (THT) instability is small when $\eta_1 \leq 10^{-6}$.

For the longitudinal motion, the longitudinal chromaticity involves the lowest non-linear part of slip factor: η_2. The bucket height and the growth time of the longitudinal head-tail (LHT) instability are both proportional to η_1/η_2. Different designs of the lattice lead to very different results for the geometry of bucket and the collective effects. It is assumed here that the contributions of η_2 and η_3 to the dynamics are sufficiently small, even if $\eta_1 = 10^{-7}$, that they can be neglected [8]. Simulations indicate that the longitudinal head-tail instability can be controlled by not allowing η_2/η_1 to become too large. Detailed studies of the acceptable parameter ranges are underway.

4 DAMPING MECHANISMS

Since the synchrotron radiation damping is negligible and the ring is quasi-isochronous (so that the effect of Lan-

dau damping is very small), neither of these are likely to damp collective instabilities. "External" mechanisms, such as BNS damping, may be needed to cure the instabilities. The BNS damping can be achieved by a radio frequency quadrupole (RFQ), which introduces a betatron tune spread across the bunch such that the bunch tail experiences a larger betatron focusing than the bunch head [6]. Fig. (3) shows that the BBU-like instability is stabilized when a small BNS tune spread is applied to the beam. One should note that, the BNS damping works for the ring only when the potential-well distortion is compensated by rf phase offset, such that the bunch shape remains approximately stationary. This is because the amount of BNS tune spread obtained from the prescribed formula $\Delta\nu_\beta(z)/\nu_\beta = \Upsilon(z)/\pi\nu_\beta$, involves the bunch's density profile. To maintain the correct BNS detuning condition, the bunch shape should not seriously deviate from its initial state; otherwise, one needs to adjust the BNS tune spread accordingly. Investigations are underway to determine if such an rf quadrupole is feasible. In addition, the transverse chromaticity, which causes betatron tune spread, may provide some Landau damping of the instability.

5 CONCLUSIONS

Various single bunch collective effects have been examined. The longitudinal microwave instability is, at present, seen to be the greatest threat to maintaining the bunch length. Operation at $\eta_1 = 10^{-7}$ is being considered, along with ideas for compensating the energy variation induced by the longitudinal wake. The transverse strong head-tail instability with the small η is seen to be BBU-like and can be stabilized by BNS damping. Other instabilities are not believed to be severe over the short storage times.

Acknowledgment

The authors are grateful to Jack Peterson and Al Garren for their helpful discussions.

6 REFERENCES

[1] P.B. Wilson, *SLAC-PUB-2884*, 1982.

[2] A. Mosnier, DAPNIA-SEA-92-06, CE Saclay.

[3] J. Peterson, private communications.

[4] S. Krinsky and J.M. Wang, Particle Accelerators, vol. 17, pp. 109-139, 1985.

[5] K.Y. Ng, Proceedings of the 9th Advanced ICFA Beam Dynamics Workshop, Ed. J.C. Gallardo, AIP Press, pp. 224-233, 1995. W.-H.Cheng, A.M. Sessler and J.S. Wurtele, Proceedings of the 9th Advanced ICFA Beam Dynamics Workshop, Ed. J.C. Gallardo, AIP Press, pp. 206-217, 1995.

[6] A. W. Chao, *Physics of Collective Beam Instabilities in High Energy Accelerators*, (John Wiley & Sons, 1993).

[7] C. Pellegrini, Nuovo Cimento 64A, 447 (1969). B. Chen and A. W. Chao, Particle Accelerators, vol. 43(1-2), pp. 77-91,1993.

[8] A. Garren, private communications.

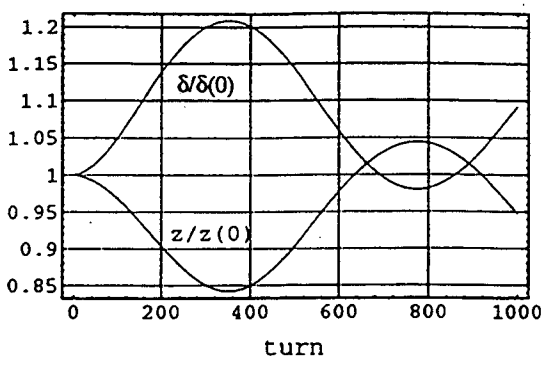

Figure 1: Scaled rms bunch size and rms energy-spread vs. turn, where at injection: $z(0) = 3$mm, $\delta(0) = 0.15\%$. Note that, $\eta_1 = 10^{-6}$ and $\eta_2 = \eta_3 = 0$.

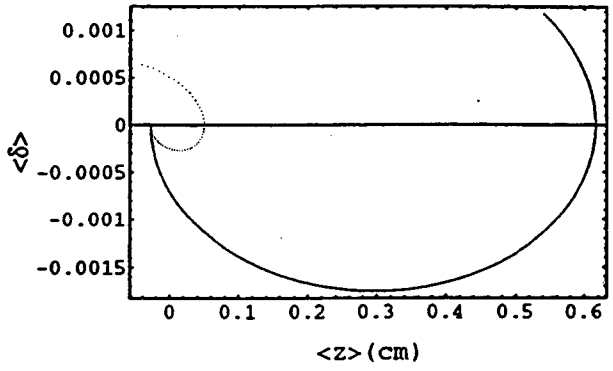

Figure 2: Center of energy-spread vs. center of bunch size. The rf phase offsets are, $\phi = 0, 0.082$ radian, for the solid line and dashed line, respectively. Note that, $\eta_1 = 10^{-6}$ and $\eta_2 = \eta_3 = 0$.

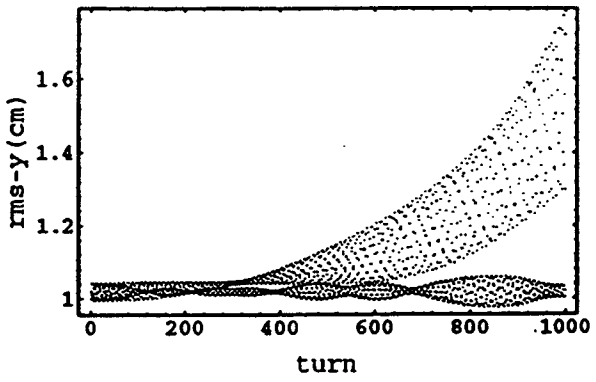

Figure 3: Blows up of the rms beam size, due to the BBU-like effect, where $1/\nu_s = 1784$. Note that $R_s/Q = 18225(\Omega)$, $b_{cavity} = 1.3$cm for the resonator model, injection error $\Delta y = 0.2$cm, and $\Upsilon(1\sigma_z) \simeq 0.017$. After BNS damping is applied, $\Delta\nu_\beta(1\sigma_z)/\nu_\beta \simeq 6 \times 10^{-5}$, the beam size fluctuates only slightly around 1 cm, a nominal injection beam size.

Ernest Orlando Lawrence Berkeley National Laboratory
One Cyclotron Road | Berkeley, California 94720

Prepared for the U.S. Department of Energy under Contract No. DE-AC03-76SF00098